

Chiral TeraHertz surface plasmonics⁰

Ian Aupiais¹, Romain Grasset¹, Dmitri Daineka², Javier Briatico³, ¹
Luca Perfetti¹, Jean-Paul Hugonin⁴, Jean-Jacques Greffet⁴, Yannis Laplace¹ ¹

¹ LSI, CEA/DRF/IRAMIS, CNRS, Ecole Polytechnique, Institut Polytechnique de Paris, Palaiseau, France

² LPICM, CNRS, Ecole Polytechnique, Institut Polytechnique de Paris, Palaiseau, France

³ Unité Mixte de Physique, CNRS, Thales, Université Paris Saclay, 91767 Palaiseau, France

⁴ Université Paris-Saclay, Institut d'Optique Graduate School, CNRS, Laboratoire Charles Fabry, 91127 Palaiseau, France

arXiv:2404.15270v1 [physics.optics] 23 Apr 2024

Abstract

Chiral engineering of TeraHertz (THz) light fields and the use of the handedness of light in THz light-matter interactions promise many novel opportunities for advanced sensing and control of matter in this frequency range. Unlike previously explored methods, this is achieved here by leveraging the chiral properties of highly confined THz surface plasmon modes. More specifically, we design ultrasmall surface plasmonic-based THz cavities and THz metasurfaces that display significant and adjustable chiral behavior under modest magnetic fields. For such a prototypical example of non-Hermitian and dispersive photonic system, we demonstrate the capacity to magnetic field-tune both the poles and zeros of cavity resonances, the two fundamental parameters governing their resonance properties. Alongside the observed handedness-dependent cavity frequencies, this highlights the remarkable ability to engineer chiral and tunable radiative couplings for THz resonators and metasurfaces. The extensive tunability offered by the surface plasmonic approach paves the way for the development of agile and multifunctional THz metasurfaces as well as the realization of ultrastrong chiral light-matter interactions at low energy in matter with potential far-reaching applications for the design of material properties.²

Introduction³

Despite its long history, the role of chirality in light-matter interactions remains intriguing, drawing intense focus both from a fundamental perspective [1, 2] and for its technological applications in sensing and controlling matter across diverse length scales, energy scales and scientific disciplines [3, 4, 5, 6, 7, 8]. In this context, the design of chiral optical fields and optically-active devices at THz frequencies holds particular significance for sensing applications across a large class of systems. This stems from the wide range of excitations exhibiting chirality within this frequency band, spanning from chemically and biologically relevant excitations in molecules [9, 10] to quantum collective modes such as magnons [4, 11, 12] and phonons [12, 13, 14] in condensed matter systems. Alongside sensing capabilities, the ultrastrong interaction between matter and chiral optical fields at

low energies has recently emerged as a new paradigm for manipulating material properties through Floquet engineering [15, 16, 17] and has been proposed to realize novel phases of matter through hybridization with the vacuum field of chiral cavities [18, 19, 20, 21, 22]. Notably, the potential to induce magnetism and non-trivial topologies in otherwise non-magnetic and topologically trivial materials [18, 21, 23], or photon condensation in the ground state [24], represent some of the most far-reaching prospects enabled by chiral vacuum fields. For these reasons, the ability to engineer ultrastrong and chiral light-matter interactions at THz frequencies, achievable through the design of cavities with ultrasmall mode volumes, appears as a new frontier in the THz range [25] that would open up many avenues for chiral sensing and matter manipulation with applications in chemistry, biology and physics.⁴

In the past years, large efforts have been devoted to the design of chiral and optically-active devices for polarization control of THz light [26, 27, 28, 29, 30, 31, 32, 33, 34]. These have been obtained following mostly two distinct routes. The first one is a synthetic or metamaterial-like approach, in which the geometric chirality of metallic resonators is tailored and transferred onto the resonating electromagnetic (EM) fields [26, 27, 28, 29, 30, 31]. The second approach relies on the natural magneto-optical activity of the bulk of semiconductors [32, 33, 34] and is enabled by the propagation of THz magneto-plasma waves [35, 36]. The latter originate from the microscopic Lorentz force acting on carriers with low effective mass m^* , giving rise to a cyclotron frequency $\nu_c = eB/2\pi m^*$ that falls within the THz frequency range for moderate magnetic fields below 1T [37]. Yet, achieving high EM-field confinement sufficient enough to reach the ultrastrong coupling regime of light-matter interaction represents to date a challenge for both of these approaches. On the one hand, shrinking the size of metallic resonators while preserving operating frequencies in the THz range is a difficult task that often requires the design of complex and technologically challenging resonator architectures [38, 39, 40]. On the other hand, utilization of magneto-plasma waves necessitates light propagation through the bulk of the semiconductor and hence only offer sizeable chiral effects at the expense of large interaction volumes [34, 36].⁴

Here, we overcome these challenges by exploiting THz surface

plasmons-based cavities in semiconductors. As demonstrated recently [41], this approach allows to downscale cavity dimensions at fixed operating frequencies and provide an efficient way to confine THz EM-fields down to the ultimate limit allowed by plasmonics. In this work, we show that surface plasmons inherit the chiral activity of the bulk and use this as a means to create chiral THz cavities with ultrasmall mode volumes. When assembled together, arrays of such cavities lead to a novel type of chiral THz metasurfaces, fully tunable by geometry, magnetic-field and even temperature. This work opens the door to exciting perspectives for the exploration of ultrastrong chiral light-matter interactions at low energies in matter.

Working principle of the chiral THz surface plasmonic cavities

In the Faraday configuration, where a homogeneous magnetic field $\mathbf{B} = Bz$ is perpendicular to the plasmonic medium's interface and a plane wave is incident normally, the magnetic field acts exclusively onto the spin-sector of the EM-field (i.e. its polarization state) and normal modes correspond to left- and right-circularly polarized (LCP/RCP) photons $E_{\sigma\pm} = e^{ik_z z} e^{-i\omega t} |\sigma\pm\rangle$ [35]. Interaction between light and the plasma involves two distinct magneto-plasmonic permittivities $\epsilon_{\sigma\pm}(\nu, B)$ and results in reflection coefficients denoted as $\tilde{r}_{\sigma\pm}(\nu, B)$ (see supplementary information).

Normal incidence experimental power reflectivity spectra $R_{\sigma\pm}(\nu) = |\tilde{r}_{\sigma\pm}(\nu, B)|^2$ as well as the phase $\phi_{\sigma\pm}(\nu, B) = \text{Arg}(\tilde{r}_{\sigma\pm}(\nu, B))$ accumulated by the electric field of the light upon reflection onto the THz plasma of bulk semiconductor InSb are shown in Fig. 1a for $\sigma\pm$ polarizations. As the cyclotron frequency ν_c varies, the THz plasma edge initially located at $\nu \approx \nu_p$ splits into two different plasma edges. Their frequencies $\nu_{p,\sigma\pm} \approx \frac{1}{2} \sqrt{4\nu_p^2 + \nu_c^2 \pm \nu_d}$ depend on the polarization handedness (see Fig. 1a-b) and highlights the bulk chirality of the plasmonic medium [35, 36].

In contrast to plane waves, where orbital and spin components of the EM-field are independent, the normal modes of the proposed ultrasmall chiral THz cavity illustrated in Fig. 1c are sustained by surface plasmons and their orbital and spin degrees of freedom are intertwined within the highly subwavelength volume of the resonator, leading to a more complex chiral behavior. This can be seen in Fig. 1d where we present the characteristics of the normal modes of circular patch cavities, which, owing to their cylindrical symmetry, represent a natural choice of plasmonic resonators in the present context. In the absence of magnetic field, their normal modes have been studied previously [42] and are characterized by an orbital angular moment L ($L = \dots, -2, -1, 0, 1, 2, \dots$) and a radial number n ($n = 1, 2, \dots$). For lossless cavities, modes of opposite orbital momentum are time-reversal symmetric of one another ($\tilde{\mathbf{E}}_{n,-L} = \tilde{\mathbf{E}}_{n,L}^*$) and hence have degenerate frequencies $\nu_{n,L} = \nu_{n,-L}$. In Fig 1d, we display the EM-fields sustained by the surface plasmon inside the resonator for a set of representative (n, L) modes: 1) the normal component of the electric field ($\text{Re}(\tilde{E}_z)$) and 2) the relative density $\Delta\sigma_{n,L}(r) = \sigma_{+,n,L}(r) - \sigma_{-,n,L}(r)$ of the

σ_+ polarized photons (or spin density of the mode), where $\sigma_{\pm,n,L}(r) \propto |E_x \pm iE_y|^2$ depends only on the radial coordinate r .

Notably, normal modes are seen to consist in a spatially dependent superposition of σ_\pm polarized photons which entails the mixing of orbital and spin degrees of freedom of the resonator. It is possible to estimate the shifts $\delta\nu_{n,L}$ of the resonance frequencies $\nu_{n,L}$ by applying a modal perturbation theory, which, to first order in ν_c , gives (see supplementary material):

$$\frac{\delta\nu_{n,L}}{\nu_{n,L}} \propto \nu_c \left(\int_0^{s/2} r \Delta\sigma_{n,L}(r) dr \right)$$

indicating that the frequency shift is proportional to the spatially integrated spin density $\Delta\sigma_{n,L}(r)$ of the σ_\pm polarized photons (s being the diameter of the patch). As depicted in Fig. 1e, the $L = 0$ mode doesn't experience any shift as it is linearly polarized, while modes with finite orbital angular momentum ($L \neq 0$) split symmetrically according to $\delta\nu_{n,L} = -\delta\nu_{n,-L}$ as they have opposite spin densities of equal magnitude. Because they carry the largest spin polarization among all, the $(n = 1, L = \pm 1)$ modes are expected to provide the most pronounced mode splitting and hence the largest chiral effect.

Sample architecture and plasmonic resonances without magnetic field

Rather than an isolated cavity, our samples consist in two-dimensional and subwavelength periodic arrays (period $s+a$) of circular patch cavities of diameter s (Fig. 2a). Over a bulk wafer of semiconducting InSb, we deposit an insulating layer of highly subwavelength thickness d (Si_3N_4 with $d \ll \lambda_0, \lambda_0$ being the wavelength in vacuum) followed by circular patches of metallic gold on top. In the absence of magnetic field and due to the four-fold symmetry of the structure, reflectivity spectra are independent of the incoming THz light polarization. In Fig. 2b, we present the experimental and simulated power reflectivity spectra for three samples having circular patches of varying diameters. The major absorption observed at low frequency corresponds to the resonance frequency of the two degenerate $(n, L) = (1, \pm 1)$ cavity modes, as confirmed by inspection of the mode profile obtained from numerical simulations (Fig. 2c). A second pronounced absorption at high frequency lies slightly below the THz plasma edge. As seen in Fig. 2c, it corresponds to the resonance of a pair of degenerate plasmonic modes that are fully expelled from the volume encompassed by the cavities and that are located between them. These modes are the counterpart in these structures of the inter-cavity mode observed in striped lattices of plasmonic cavities [41]. For completeness, we also report the presence of: 1) a small absorption for the $s = 43\mu\text{m}$ sample (triangle in Fig. 2b) which corresponds to the excitation of the higher order $(n, L) = (3, \pm 1)$ cavity modes and whose mode profile is shown in Fig. 2c and 2) a resonance corresponding to the excitation of a continuum of propagating bulk plasma modes within the transparency region of the plasmonic medium arising the first-order diffraction of the array ($s = 43\mu\text{m}$ sample, star in Fig. 2b). In the remaining of this

paper, we will not further discuss the latter resonances and will focus our analysis on the main cavity resonance. 11

Surface plasmonic chirality and its magnetic field dependence 12

Upon application of the magnetic field, we observe the lifting of the degeneracy of the $(n, L) = (1, +1)$ and $(1, -1)$ cavity resonance. This is featured in the polarization resolved THz spectra presented in Fig. 3a-b-c as two frequency-displaced resonant absorptions for opposite σ_{\pm} polarizations, hence demonstrating the chiral effect that is looked for. 13

Besides the polarization handedness-dependent frequency-shifts, we notice that the contrast of the cavity resonance varies strongly and evolves oppositely for opposite σ_{\pm} polarizations. The large variation of its contrast can be inferred from the value of the reflectivity minimum at resonance R_{min} which changes as much as $\sim 50\%$ within the range of parameters investigated (see top and bottom panels in Fig. 3a-b-c). This observation suggests that the magnetic field is acting to tune another crucial cavity parameter: the overall coupling efficiency of external radiation to the cavity. It can be understood qualitatively from temporal coupled mode theory [43] which predicts that $R_{min} = (\Gamma_r - \Gamma_{\Omega})^2 / (\Gamma_r + \Gamma_{\Omega})^2$ for single-port cavities [44, 45], where Γ_r and Γ_{Ω} are the radiative and non-radiative decay rates of the cavity describing respectively the coupling of the resonator to external radiation and the decay of the resonance due to ohmic losses. In other words, R_{min} measures how close the cavity is from critical coupling at which $\Gamma_i = \Gamma_r$ ($R_{min} = 0$) and all incident radiation is coupled and dissipated into the cavity. In order to further assess quantitatively and reliably all cavity parameters for this highly non-Hermitian and dispersive photonic system [46, 47, 48], we fitted the two quadratures of the reflection coefficient $\tilde{r}_{\sigma_{\pm}}(\nu, B)$ based on an analytical continuation of the frequency in the complex plane [49, 50, 51] ($\nu \rightarrow \tilde{\nu}$ and $\tilde{r}_{\sigma_{\pm}}(\nu, B) \rightarrow \tilde{r}_{\sigma_{\pm}}(\tilde{\nu}, B)$, see supplementary material). This leads to a pole-zero representation of the cavity resonance shown in Fig. 4a. We define the complex zero $\tilde{\nu}_{z0}$ by the condition $\tilde{r}_{\sigma_{\pm}}(\tilde{\nu}_{z0}) = 0$. Following this zero in the complex plane enables to characterize the undercoupled ($Im(\tilde{\nu}_{z0}) < 0$), critically coupled ($Im(\tilde{\nu}_{z0}) = 0$) and overcoupled ($Im(\tilde{\nu}_{z0}) > 0$) regimes. Note that the critically coupled regime is closely linked to the coherent perfect absorption [52, 53, 54]. We observe that as the magnetic field is raised, the zero either moves towards (σ_-) the real axis (critical coupling) or departs from it (σ_+), signaling not only the tunability of the coupling but also its chiral behavior. The major results of the analysis of the cavity parameters are further presented in Fig. 4b. 13

The relative frequency-shifts of the cavity resonance are defined as $\frac{\delta\nu_0}{\nu_0} = \frac{\nu_{0,\sigma_{\pm}}(B) - \nu_0(B=0)}{\nu_0(B=0)}$ 13 where $\nu_{0,\sigma_{\pm}}(B) = Re(\tilde{\nu}_{0,\sigma_{\pm}}(B))$ corresponds to the real part of the cavity pole $\tilde{\nu}_{0,\sigma_{\pm}}(B)$, i.e. the cavity resonance frequency. As anticipated, we observe that they demonstrate opposite variations for σ_{\pm} polarizations as a function of magnetic field B . While linear in B at small fields, they acquire a slight quadratic dependence at larger fields which is reminiscent of the dependences of bulk magneto-plasma modes [36]. At $B = 500mT$, the relative shifts amount to 14%, 20% and 24% for the 21, 32

and $43\mu m$ cavities respectively in between the two σ_{\pm} polarizations. The two decay rates, determined from the knowledge of the pole and the zero as $\Gamma_{\Omega} = -Im(\tilde{\nu}_0 + \tilde{\nu}_{z0})/2$ and $\Gamma_r = -Im(\tilde{\nu}_0 - \tilde{\nu}_{z0})/2$ (see supplementary material), also evolve as a function of magnetic-field and exhibit chiral behaviour: $\Gamma_{r/\Omega,\sigma_{+}}(B) \neq \Gamma_{r/\Omega,\sigma_{-}}(B)$. While this is somewhat expected for the ohmic decay rate as the cyclotron resonance modulates material dissipation in the vicinity of $\nu = \pm\nu_c$, the most striking feature is the chiral and large variations observed for the radiative decay rate by as much as 300% in the range of parameters investigated. Such phenomenon is largely unexpected as this quantity is generally believed to depend solely on geometrical parameters of the arrays [44, 45, 55]. We attribute it to the magnetic field-tuning of the phase $\phi_{\sigma_{\pm}}(\nu, B)$ accumulated by the THz fields upon reflection onto the underlying plasmonic medium. More specifically, denoting $\tilde{r}_{\sigma_{\pm},0}(\nu, B)$ the background reflectivity of the structure *in the absence of metallic patches* (i.e. involving only the *vacuum/Si₃N₄/InSb* planar multilayer), we show that the variation of the radiative decay rate can be well reproduced and explained by a functional dependence of the form $\Gamma_{r,\sigma_{\pm}}(B) = \alpha |1 + \tilde{r}_{\sigma_{\pm},0}(\nu, B)|^2$ where $\tilde{r}_{\sigma_{\pm},0}(\nu, B)$ is evaluated at the *vacuum/Si₃N₄* interface, at the cavity resonance frequency $\nu = \nu_{0,\sigma_{\pm}}(B)$, and α is a geometry-dependent but magnetic field-independent scaling factor (black solid lines in Fig. 4b). Such a relation between background reflectivity and radiative decay rates has been derived analytically for metal/insulator/metal cavities in a context where the phase did not play any significant role [56, 57]. In the present case however, the phase $\phi_{\sigma_{\pm}}(\nu, B)$ of the reflected field is the central parameter controlling such behavior, as within a good approximation $|\tilde{r}_{\sigma_{\pm},0}(\nu, B)| \approx 1$, so that $\Gamma_{r,\sigma_{\pm}}(B) \propto \cos(\phi_{\sigma_{\pm}}(\nu, B)/2)^2$. The basic idea behind the tunability and chirality of the radiative decay rates that we observe is sketched in Fig. 4c. In the absence of metallic patches, interference of the incident $E_{i,\sigma_{\pm}}$ and reflected fields $E_{r,\sigma_{\pm}} = \tilde{r}_{\sigma_{\pm},0}(\nu, B)E_{i,\sigma_{\pm}}$ result in a total background field of amplitude $|E_{tot,\sigma_{\pm}}| = |1 + \tilde{r}_{\sigma_{\pm},0}(\nu, B)| |E_{i,\sigma_{\pm}}|$ that takes the form of a standing wave whose locations of nodes and anti-nodes are crucially depending the phase $\phi_{\sigma_{\pm}}(\nu, B)$ accumulated upon reflection from the plasmonic medium. Immersed into this background field, the metallic patches in- and out-couple it to the cavity with coupling rates $\sqrt{2\Gamma_{r,\sigma_{\pm}}(B)}$ [43] being determined by the field amplitude at their location and hence scaling as $|1 + \tilde{r}_{\sigma_{\pm},0}(\nu, B)|$. This leads to an overall radiation decay rate given by: $\Gamma_{r,\sigma_{\pm}}(B) \propto |1 + \tilde{r}_{\sigma_{\pm},0}(\nu, B)|^2$. This phenomenon is analogous to a resonant nanoparticle located at distance L above a metallic mirror and whose coupling to external radiation $\Gamma_r \propto \sin(2\pi L/\lambda_0)^2$ is adjustable by varying the location of the nanoparticle with respect to the standing wave (see Fig. 4d). Here, despite the fixed geometry, the sizeable variations of the phase provided by the underlying plasmonic medium close to the plasma frequency as well as their tunability with magnetic field play the same role as the height for the nanoparticle. 13

As such, for the proposed plasmonic cavities, we demonstrate that chirality proceeds not only by frequency splitting of degenerate modes but also by a chiral and tunable coupling of the resonators to external radiation. This constitutes an important result of this study. 13

Chiral THz surface plasmonic metasurfaces¹⁴

We discuss here an application where the proposed structures can be exploited as resonant and tunable reflective THz chiral metasurfaces for polarization control of the THz light. In order to demonstrate the advantages of structuring a metasurface over that of using a bulk semiconductor for this purpose, we compare in Fig. 5 the optical activity of the unstructured bulk material and that of a structured metasurface. Optical activity is commonly characterized in terms of: 1) circular dichroism (CD) via the ellipticity $\eta = \frac{|r_{\sigma_+}(\nu)| - |r_{\sigma_-}(\nu)|}{|r_{\sigma_+}(\nu)| + |r_{\sigma_-}(\nu)|}$ and 2) optical rotary dispersion (OR) via the rotation angle $\theta = \frac{\phi_{\sigma_+}(\nu) - \phi_{\sigma_-}(\nu)}{2}$ [58]. For linearly polarized incident light, CD and OR result in the present context in reflected light that is elliptically polarized (CD phenomenon) and rotated by an angle θ compared to the incident polarization (OR phenomenon), see Fig. 5a. In Fig. 5b, we compare the ellipticity and optical rotation angle of the bulk and structured metasurface at $B = 500mT$.¹⁵

We notice profound differences between the two responses. Firstly, we observe that CD and OR of the bulk material display rather complex shapes in an otherwise large frequency window centered around the plasma edge. This results in overall poor spectral control of the optical activity of the bulk material. In contrast, the ellipticity of the metasurface presents two sizeable peaks of opposite polarity at around 1THz and 2THz, which correspond to the frequencies of the cavity and intercavity resonances respectively for this $s = 32\mu m$ cavity metasurface. Ellipticity around the cavity resonance demonstrates in particular a well-defined unipolar behaviour.¹⁵

Strikingly, at the cavity resonance, the ellipticity reaches a sizeable value $\eta \approx 0.5$ that is at a frequency where the bulk ellipticity is almost null within noise level: this corresponds to a giant enhancement of the ellipticity provided by the metasurface. The ability to induce such a large dichroism in a frequency band well below the plasma frequency where the bulk material only provides a minute effect demonstrates the superiority of metasurface over the bulk material for the chiral engineering of THz light fields. The origin of such a metasurface-enabled ellipticity can be traced back to the difference in the contrast between σ_+ and σ_- resonances. In this respect, chirality of the radiative decay rates of the cavities discussed in the previous section is crucial in providing this effect.¹⁵

In the supplementary material, we further show the wide tunability of the optical activity of the metasurfaces both spectrally via the geometrical tuning of the cavity dimensions and in its magnitude via the tuning of the magnetic field strength. Such metasurfaces achieve ellipticities as high as $\eta \approx 0.7$ at a moderate field $B = 500mT$ relevant for applications, and we expect that full ellipticity ($\eta = 1$) is reachable around $600 - 700mT$.¹⁵

Discussion¹⁶

Our approach offers a major and unique asset with respect to other alternatives for the chiral engineering of THz fields based on either synthetic [26, 28, 29, 31] or natural [36, 32, 34] optical activity. In comparison, the large magnitude of optical activity obtained here is achieved over much smaller, i.e. deep-subwavelength, scales thanks to the remarkable confinement properties of surface plasmons. All the reported chiral effects originate from beneath the surface of the plasmonic medium within the penetration depth of the surface plasmons that is $\sim 0.01\lambda_0$ (where λ_0 is the free space wavelength) and within cavities with mode volumes of the order of $10^{-6}\lambda_0^3$. This represents at least two orders of magnitude enhancement over previous approaches for typical figure of merits that compare the magnitude of CD/OR and the lenght or volume over which it is realized. Straightforward improvements can be readily achieved by reducing cavity mode volumes to $10^{-8}\lambda_0^3$ [41] or by increasing the ratio ν_c/ν_p through the magnetic field or the temperature [41], as this ratio governs the overall magnitude of the chiral effects. In summary, along with the numerous opportunities it allows for harnessing ultrastrong chiral light-matter interactions for the sensing and control of matter at THz frequencies, this system stands out as a singular platform within the electromagnetic spectrum for unravelling novel phenomena in chiral plasmonics thanks to the extended parameter space in ν_c/ν_p which remains beyond reach at mid-infrared and optical frequencies.¹⁷

Acknowledgments¹⁸

L.Y. acknowledges support from Agence Nationale de la Recherche (grant n° ANR- 17-CE30-0011-11) and Labex PALM (grant n° ANR-10-LABX-0039-PALM).¹⁹

Methods²⁰

Sample manufacturing²¹

Samples were manufactured starting from a $500\mu m$ thick, $< 100 >$ oriented, bulk wafer of InSb commercially available (MTI Corporation). The InSb wafer was nominally N-type undoped. Each sample consisted of a $\sim 5 mm * 5 mm * 0.5 mm$ InSb substrate dice-cut from the wafer. An insulating layer of Si_3N_4 was deposited via plasma enhanced chemical vapor deposition and the top metallic patches were realized via photolithography followed by metal deposition of $Ti(15 nm)/Au(200 nm)$. The geometric and optical parameters of the samples are provided in the supplementary information.²²

THz spectroscopy²³

Spectroscopy of the samples was performed with a time-domain THz spectrometer driven by an ultrafast Ti:Sapphire oscillator. THz generation and detection were achieved via a photoconductive emitter (Tera-SED) and a $1 mm$ thick $< 110 >$ ZnTe crystal, respectively, allowing for spectroscopic coverage from 0.2 THz to 2.5 THz. Delayed THz pulses originating from the optical components of the setup were elimi-

nated by windowing the main THz pulse reflected off the samples. The time domain signals were Fourier transformed and analyzed in both their amplitude and phase. All reflectivity measurements were conducted at normal incidence and room temperature. For absolute measurements of the reflectivity, we used the THz pulse reflected off a gold-coated sample as a reference. In all measurements, the THz spot size ($\sim 2 \text{ mm}$ in diameter) is well below the size of the manufactured samples, so that the samples can be considered infinite in the plane containing the interface (x - y plane in Fig. 2.a). Polarization-resolved THz measurements were obtained by initially decomposing the linearly-polarized incident THz pulse into the σ_{\pm} circular basis. The reflection coefficient of each σ_{\pm} component was obtained thanks to a polarization-resolved detection. A description of the experimental setup and of the polarization-resolved THz measurements is reported in the supplementary information. The magnetic field was applied by a large static magnet located behind the sample and was calibrated with a Hall probe. Homogeneity of the magnetic-field and the uncertainty on its absolute magnitude were better than 3% across the THz spot size.

Numerical simulations

Numerical simulations of the cavities presented in Fig. 2b were performed with the Rigorous Coupled Wave Analysis method [59, 60]. The optical and geometrical parameters used in the simulations are determined from experimental measurements performed on the samples (see supplementary information). The permittivity of Gold at THz frequencies was taken from [61] and the permittivity of Si_3N_4 from [41].

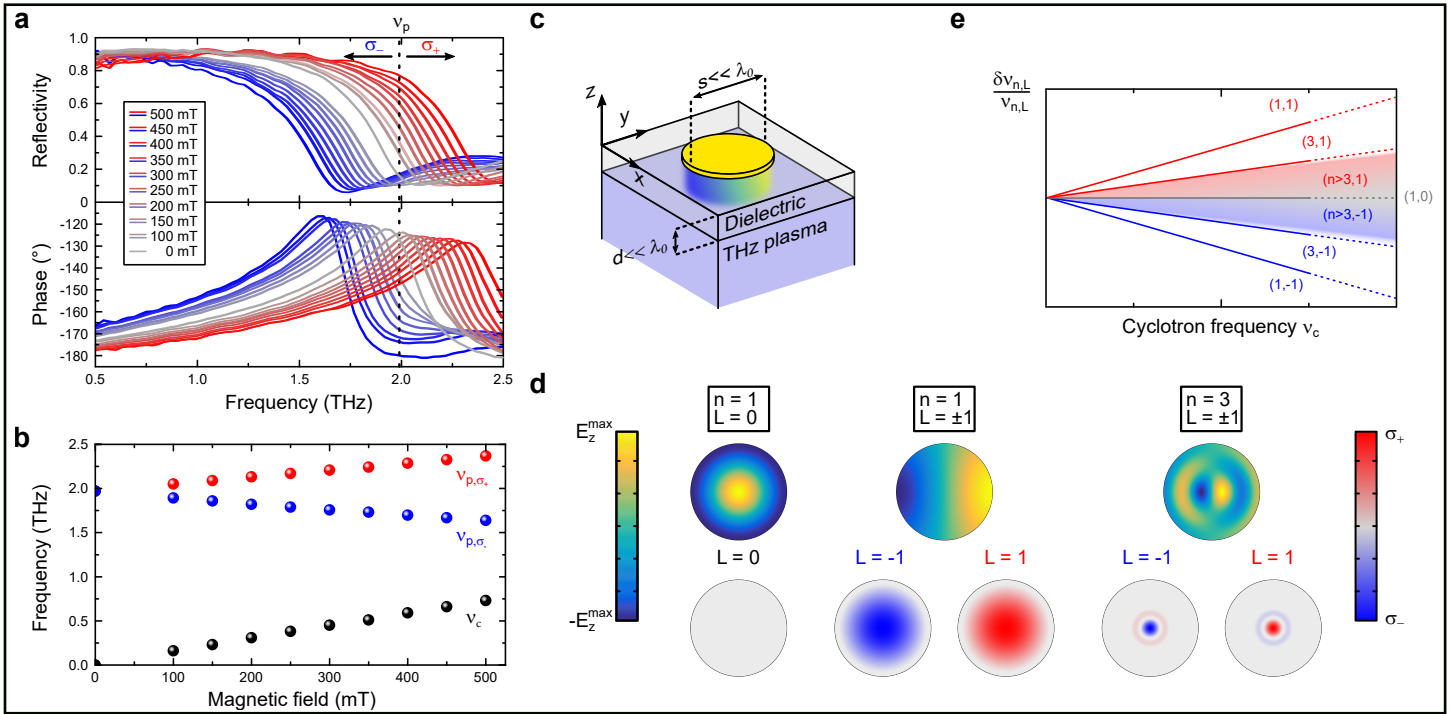


Figure 1: **a)** σ_{\pm} polarization-resolved power spectra (top panel) and phase (bottom panel) of the reflected THz field from bulk InSb at various magnetic fields between 0 mT and 500 mT. Measurements are performed at normal incidence and the magnetic field is applied perpendicular to the surface of the plasmonic medium. The dashed line indicates the location of plasma frequency ν_p at $B = 0$ mT. **b)** Cyclotron frequency (black dots) as a function of magnetic field, determined from fitting the bulk reflectivity spectra with the magneto-plasmonic model of permittivities (see also supplementary material). Red and blue dots indicate handedness-dependent plasma frequencies $\nu_{p,\sigma_{\pm}}$ associated with the cyclotron resonance active and inactive bulk magneto-plasma waves ([35]). **c)** Sketch of a single subwavelength chiral THz plasmonic cavity with overall dimensions $s, d \ll \lambda_0$. **d)** Characteristics of the plasmonic modes for some selected cavity resonances of the circular patch cavity without a magnetic field: $(n,L) = \{(1,0), (1,+1), (1,-1), (3,+1), (3,-1)\}$. Shown are color plots of: 1) the normal component of the EM-field ($Re(\tilde{E}_z)$) (top) and 2) relative density of the σ_{\pm} polarized photons (or ‘spin’ density, bottom) of the corresponding surface plasmon **e)** Resonance splitting expected for the different orbital modes of the subwavelength cavity as a function of the cyclotron frequency. 27

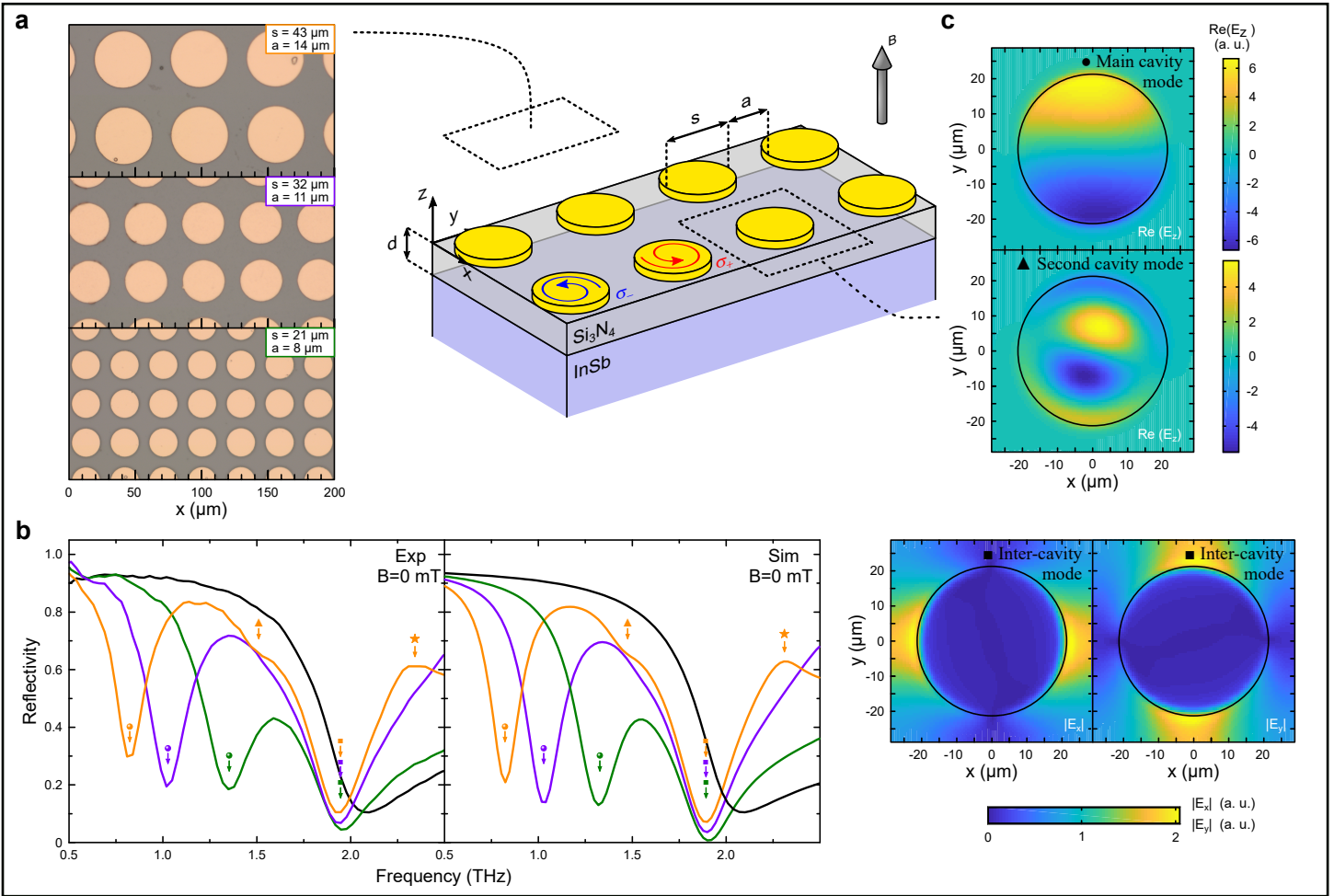


Figure 2: Figure 2: a) Sample architecture and geometrical parameters of the two-dimensional array of circular patch cavities (right). Top-view optical pictures of the actual samples (left). b) Experimental (left) and simulated (right) normal incidence THz power reflectivity spectra of the 3 samples investigated at zero magnetic field ($B = 0 \text{ mT}$): $s = 43 \mu\text{m}$ (orange solid curve), $s = 32 \mu\text{m}$ (purple solid curve), $s = 21 \mu\text{m}$ (green solid curve). The normal incidence THz power reflectivity spectrum of bulk InSb is reported for comparison (black solid curve). The different plasmonic resonances are reported: main cavity resonance (dots), second cavity resonance (triangle), intercavity resonance (squares), first-order diffraction of the array (star) c) Simulated EM mode profiles of the $s = 43 \mu\text{m}$ sample performed at frequencies corresponding to the resonances indicated in panel b. All mode profiles are shown for a z -cut taken in the middle of the dielectric insulator at $z = d/2$. Top: Mode profile of the main cavity resonance (plot of $\text{Re}(\tilde{E}_z)$). Center: Mode profile of the second cavity resonance (plot of $\text{Re}(\tilde{E}_z)$). Bottom: Mode profile of the inter-cavity resonance (plots of $|\tilde{E}_x|$ and $|\tilde{E}_y|$)

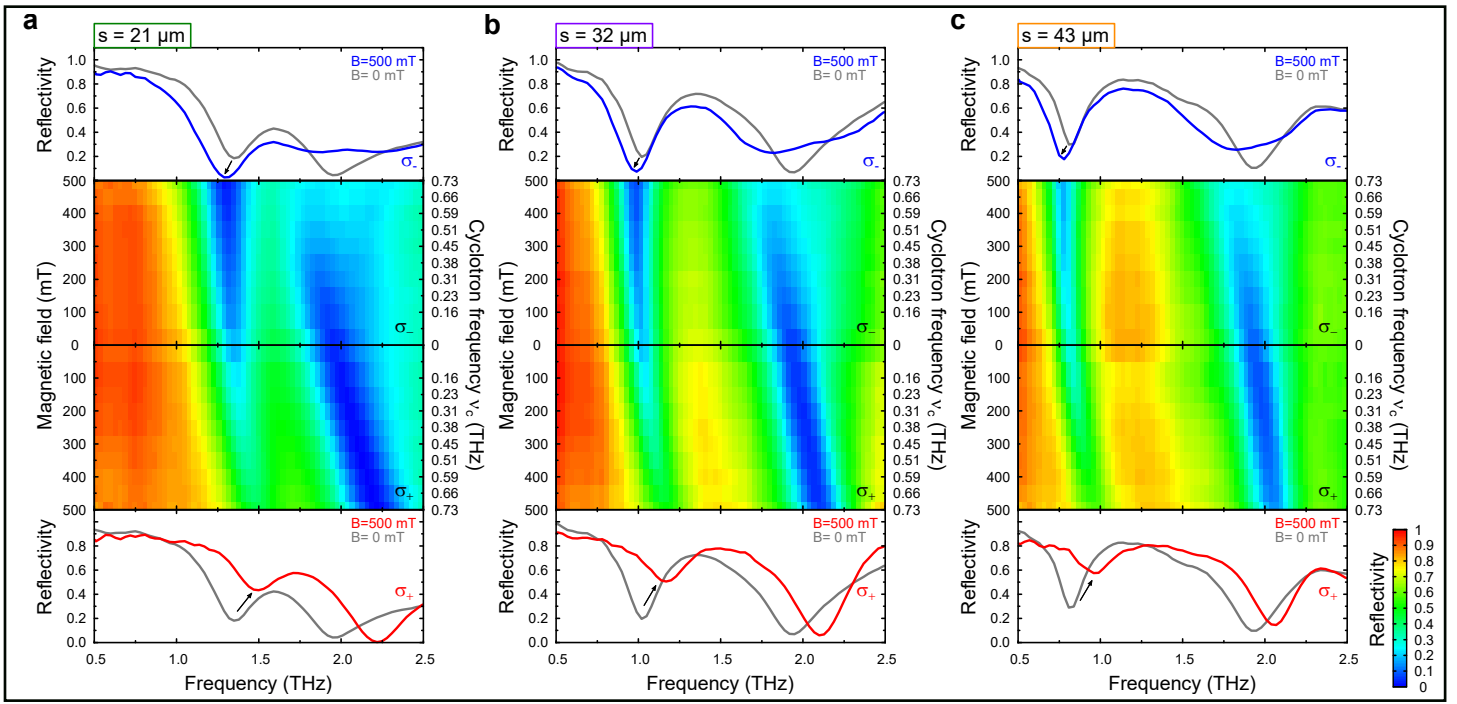


Figure 3: Experimental measurements of the σ_+ polarization-resolved THz power reflectivity spectra as a function of magnetic field between 0 mT and 500 mT for the three samples investigated: **a)** $s = 21 \mu\text{m}$ **b)** $s = 32 \mu\text{m}$ and **c)** $s = 43 \mu\text{m}$. The central panels display the THz reflectivity spectra in color scale. For each magnetic field, the corresponding cyclotron frequency is reported on the right axis. The top and bottom panels show the THz spectra at $B = 500 \text{ mT}$ obtained for the σ_+ (bottom panel, red solid curves) and σ_- (top panel, blue solid curves) polarizations, together with the THz spectrum obtained at $B = 0 \text{ mT}$ for comparison (grey solid curves).

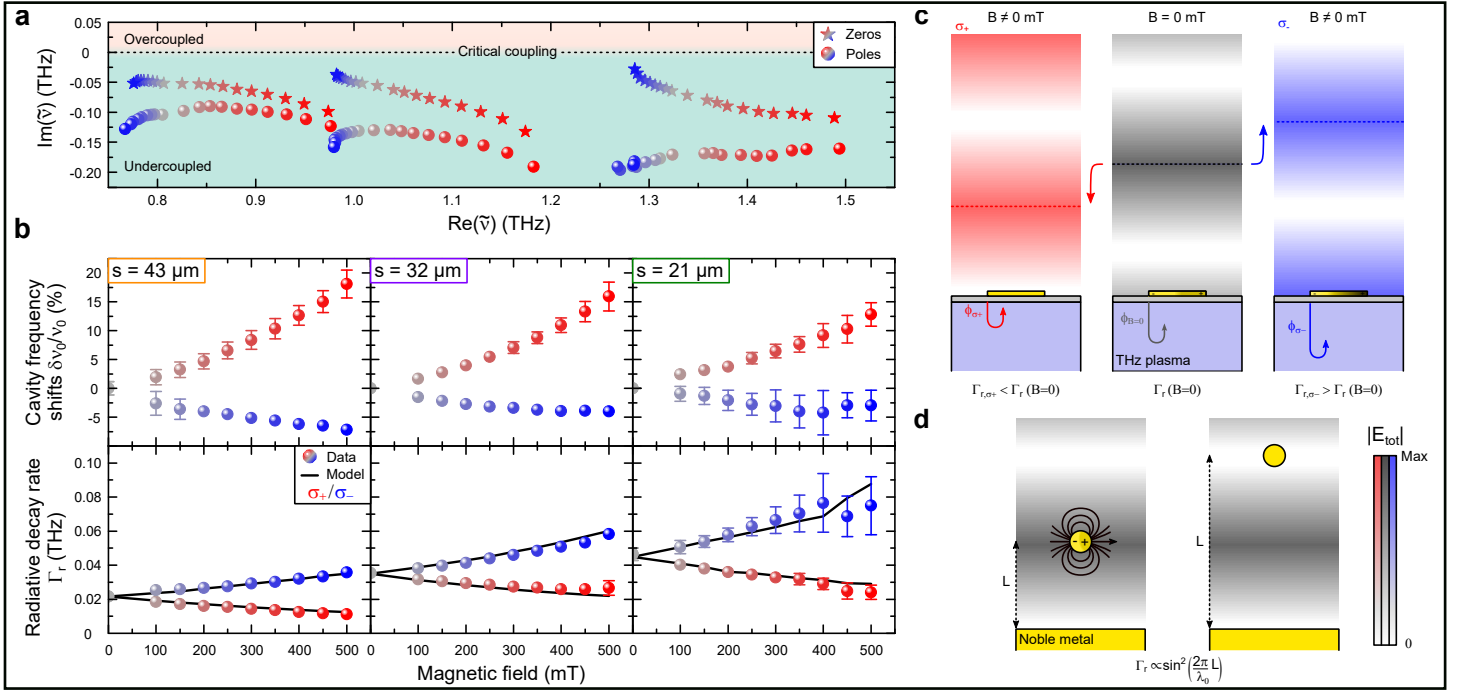


Figure 4: **a**) Location of the poles ($\tilde{\nu}_0$) and zeros ($\tilde{\nu}_{z0}$) of the cavity resonance in the complex plane and their trajectory under application of the magnetic field. **b**) Chirality of the cavity parameters as a function of magnetic field for σ_+ (red dots) and σ_- (blue dots) polarizations. Top panels: relative frequency-shifts $\delta\nu_{0,\sigma\pm}/\nu_0$. Bottom panels: radiative decay rates $\Gamma_{r,\sigma\pm}$. The experimental data (dots) is compared to the model describing the variation of the radiative decay rates in a magnetic field (black solid lines): $\Gamma_{r,\sigma+}(B) = \alpha |1 + \tilde{r}_{\sigma+,0}(\nu, B)|^2$ (see main text). From left to right: $s = 43, 32$ and $21 \mu\text{m}$ cavity samples. **c**) Sketch of the origin of the chirality and of the tuning of the radiative decay rates with the magnetic field. In the absence of the gold patch, incoming and reflected light from the plasmonic medium interfere to form standing waves with total amplitude $|E_{tot,\sigma\pm}|$ (the background field) whose location of nodes and anti-nodes depend on the phase $\phi_{\sigma\pm}(\nu, B)$ imposed by the medium upon reflection, as shown by the dashed lines which indicate the location of the anti-nodes of the background field. When the gold patch is then introduced, it acts both as a support to the cavity resonance and as a coupler to it. Its location with respect to the background field determines how much light is coupled in and out of the cavity. The chirality and tunability of the phase $\phi_{\sigma\pm}(\nu, B)$ of the bulk plasmonic medium, as shown in Fig. 1a, is hence rooting that of the radiative decay rates. **d**) Analogy of the tuning of the radiative decay rates with a resonant nanoparticle located above a metallic mirror. In the absence of the nanoparticle, incoming and reflected light from the metallic mirror form standing waves. When the nanoparticle is then immersed into this background field, its location determines the amount of light that is scattered and used to drive its resonance, i.e. the radiative decay rates. If it is located at the anti-node of the background field, the absence of light inhibits the resonance, while if it is located at a node, the resonance is maximally driven. The height of the nanoparticle controls in this case the radiative decay rates and tunability is achieved geometrically.

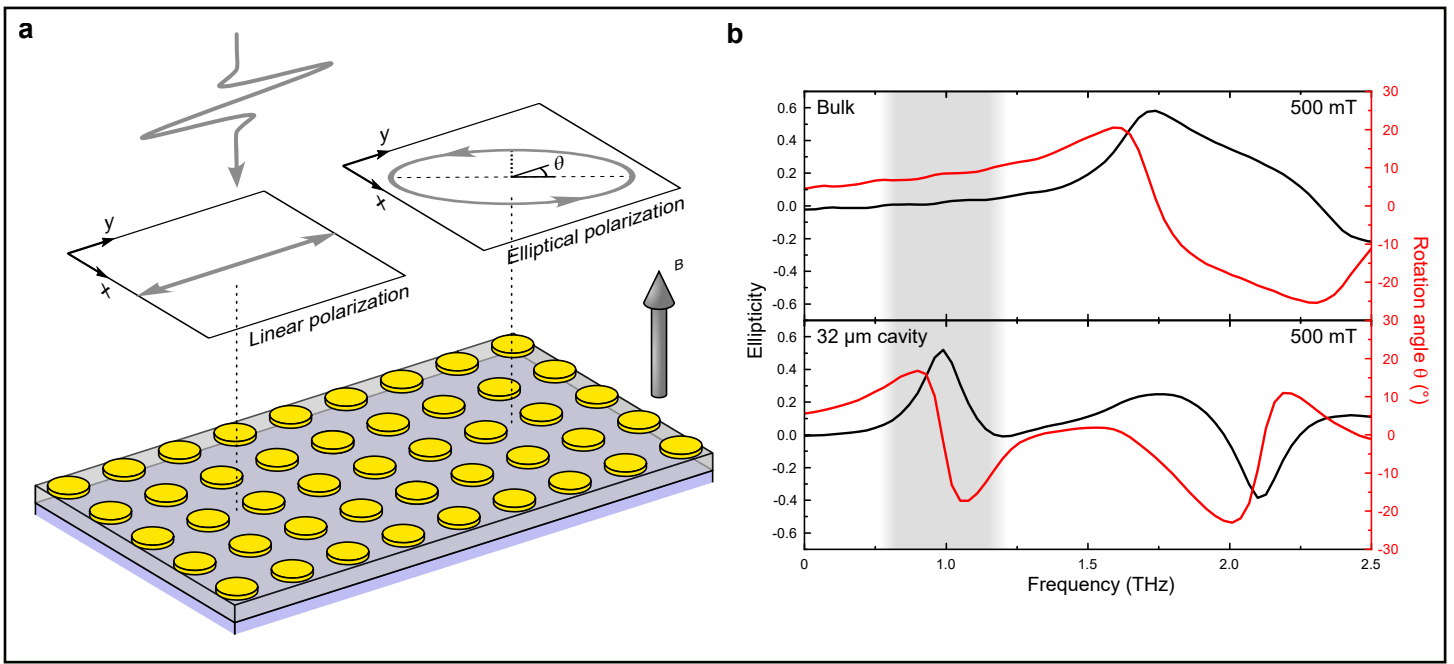


Figure 5: Comparison between the optical activity arising from the bulk semiconductor and a THz metasurface. **a** Sketch of the change in the polarization of the light as due to optical activity from either the bulk semiconductor or a structured metasurface (here shown is the metasurface). Optical activity manifests in circular dichroism (CD) and optical rotary dispersion (OD). For linearly polarized incident light, CD results in elliptical polarization while OR results in optical rotation of the polarization by an angle θ of the reflected light. **b** Comparison of CD and OR between the bulk semiconductor (top panel) and $s = 32\mu\text{m}$ metasurface (bottom panel) at $B = 500\text{ mT}$.³¹

References

- [1] Yiqiao Tang and Adam E. Cohen. Optical chirality and its interaction with matter. *Physical Review Letters*, 104(16):163901, April 2010. 32
- [2] Jungho Mun, Minkyung Kim, Younghwan Yang, Trevor Badloe, Jincheng Ni, Yang Chen, Cheng-Wei Qiu, and Junsuk Rho. Electromagnetic chirality: from fundamentals to nontraditional chiroptical phenomena. *Light: Science and Applications*, 9(1), September 2020. 33
- [3] Yiqiao Tang and Adam E. Cohen. Enhanced enantioselectivity in excitation of chiral molecules by superchiral light. *Science*, 332(6027):333–336, April 2011. 34
- [4] S. Bordács, I. Kézsmárki, D. Szaller, L. Demkó, N. Kida, H. Murakawa, Y. Onose, R. Shimano, T. Rőöm, U. Nagel, S. Miyahara, N. Furukawa, and Y. Tokura. Chirality of matter shows up via spin excitations. *Nature Physics*, 8(10):734–738, August 2012. 35
- [5] Peter Lodahl, Sahand Mahmoodian, Søren Stobbe, Arno Rauschenbeutel, Philipp Schneeweiss, Jürgen Volz, Hannes Pichler, and Peter Zoller. Chiral quantum optics. *Nature*, 541(7638):473–480, jan 2017. 36
- [6] Jochen R. Brandt, Francesco Salerno, and Matthew J. Fuchter. The added value of small-molecule chirality in technological applications. *Nature Reviews Chemistry*, 1(6), June 2017. 37
- [7] Andrew Lininger, Giovanna Palermo, Alexa Guglielmelli, Giuseppe Nicoletta, Madhav Goel, Michael Hinczewski, and Giuseppe Strangi. Chirality in light–matter interaction. *Advanced Materials*, 35(34), May 2022. 38
- [8] Cyriaque Genet. Chiral light–chiral matter interactions: an optical force perspective. *ACS Photonics*, 9(2):319–332, January 2022. 39
- [9] Won Jin Choi, Keiichi Yano, Minjeong Cha, Felipe M. Colombari, Ji-Young Kim, Yichun Wang, Sang Hyun Lee, Kai Sun, John M. Kruger, André F. de Moura, and Nicholas A. Kotov. Chiral phonons in microcrystals and nanofibrils of biomolecules. *Nature Photonics*, 16(5):366–373, mar 2022. 40
- [10] Won Jin Choi, Sang Hyun Lee, Bum Chul Park, and Nicholas A. Kotov. Terahertz circular dichroism spectroscopy of molecular assemblies and nanostructures. *Journal of the American Chemical Society*, 144(50):22789–22804, dec 2022. 41
- [11] Tobias Kampfrath, Alexander Sell, Gregor Klatt, Alexej Pashkin, Sebastian Mährlein, Thomas Dekorsy, Martin Wolf, Manfred Fiebig, Alfred Leitenstorfer, and Rupert Huber. Coherent terahertz control of antiferromagnetic spin waves. *Nature Photonics*, 5(1):31–34, nov 2010. 42
- [12] Jun Cui, Emil Viñas Boström, Mykhaylo Ozerov, Fangliang Wu, Qianni Jiang, Jien-Haw Chu, Changcun Li, Fucai Liu, Xiaodong Xu, Angel Rubio, and Qi Zhang. Chirality selective magnon-phonon hybridization and magnon-induced chiral phonons in a layered zigzag anti-ferromagnet. *Nature Communications*, 14(1), jun 2023. 43
- [13] Kyosuke Ishito, Huiling Mao, Yusuke Kousaka, Yoshihiko Togawa, Satoshi Iwasaki, Tiantian Zhang, Shuichi Murakami, Jun ichiro Kishine, and Takuya Satoh. Truly chiral phonons in α -HgS. *Nature Physics*, 19(1):35–39, oct 2022. 44
- [14] Andrey Baydin, Felix G. G. Hernandez, Martin Rodriguez-Vega, Anderson K. Okazaki, Fuyang Tay, G. Timothy Noe, Ikufumi Katayama, Jun Takeda, Hiroyuki Nojiri, Paulo H.O. Rappl, Eduardo Abramof, Gregory A. Fiete, and Junichiro Kono. Magnetic control of soft chiral phonons in PbTe. *Physical Review Letters*, 128(7):075901, feb 2022. 45
- [15] Y. H. Wang, H. Steinberg, P. Jarillo-Herrero, and N. Gedik. Observation of floquet-bloch states on the surface of a topological insulator. *Science*, 342(6157):453–457, October 2013. 46
- [16] J. W. McIver, B. Schulte, F.-U. Stein, T. Matsuyama, G. Jotzu, G. Meier, and A. Cavalleri. Light-induced anomalous hall effect in graphene. *Nature Physics*, 16(1):38–41, November 2019. 47
- [17] Gabriel E. Topp, Gregor Jotzu, James W. McIver, Leda Xian, Angel Rubio, and Michael A. Sentef. Topological floquet engineering of twisted bilayer graphene. *Physical Review Research*, 1(2):023031, September 2019. 48
- [18] Xiao Wang, Enrico Ronca, and Michael A. Sentef. Cavity quantum electrodynamical chern insulator: Towards light-induced quantized anomalous hall effect in graphene. *Physical Review B*, 99(23):235156, June 2019. 49
- [19] Hannes Hübener, Umberto De Giovannini, Christian Schäfer, Johan Andberger, Michael Ruggenthaler, Jerome Faist, and Angel Rubio. Engineering quantum materials with chiral optical cavities. *Nature Materials*, 20(4):438–442, nov 2020. 50
- [20] I. V. Tokatly, D. R. Gulevich, and I. Iorsh. Vacuum anomalous hall effect in gyrotropic cavity. *Physical Review B*, 104(8):l081408, August 2021. 51
- [21] D. D. Sedov, V. Shirobokov, I. V. Iorsh, and I. V. Tokatly. Cavity-induced chiral edge currents and spontaneous magnetization in two-dimensional electron systems. *Physical Review B*, 106(20):205114, nov 2022. 52
- [22] John Clai Owens, Margaret G. Panetta, Brendan Saxberg, Gabrielle Roberts, Srivatsan Chakram, Ruichao Ma, Andrei Vrajitoarea, Jonathan Simon, and David L. Schuster. Chiral cavity quantum electrodynamics. *Nature Physics*, 18(9):1048–1052, jul 2022. 53
- [23] Kanta Masuki and Yuto Ashida. Berry phase and topology in ultrastrongly coupled quantum light-matter systems. *Physical Review B*, 107(19):195104, May 2023. 54
- [24] Alberto Mercurio, Gian Marcello Andolina, Francesco M. D. Pellegrino, Omar Di Stefano, Pablo Jarillo-Herrero, Claudia Felser, Frank H. L. Koppens, Salvatore 55

- Savasta, and Marco Polini. Photon condensation, van vleck paramagnetism, and chiral cavities. *Physical Review Research*, 6(1):013303, March 2024. 55
- [25] Johan Andberger, Lorenzo Graziotto, Luca Sacchi, Matthias Beck, Giacomo Scalari, and Jerome Faist. Terahertz chiral metamaterial cavities breaking time-reversal symmetry. *arXiv.2308.03195*, 2023. 56
- [26] Shuang Zhang, Jiangfeng Zhou, Yong-Shik Park, Junsuk Rho, Ranjan Singh, Sunghyun Nam, Abul K. Azad, Hou-Tong Chen, Xiaobo Yin, Antoinette J. Taylor, and Xiang Zhang. Photoinduced handedness switching in terahertz chiral metamolecules. *Nature Communications*, 3(1), jul 2012. 57
- [27] Jianfeng Wu, Binghao Ng, Haidong Liang, Mark B.H. Breese, Minghui Hong, Stefan A. Maier, Herbert O. Moser, and Ortwin Hess. Chiral metafoils for terahertz broadband high-contrast flexible circular polarizers. *Physical Review Applied*, 2(1):014005, July 2014. 58
- [28] Tetsuo Kan, Akihiro Isozaki, Natsuki Kanda, Natsuki Nemoto, Kuniaki Konishi, Hidetoshi Takahashi, Makoto Kuwata-Gonokami, Kiyoshi Matsumoto, and Isao Shimoyama. Enantiomeric switching of chiral metamaterial for terahertz polarization modulation employing vertically deformable MEMS spirals. *Nature Communications*, 6(1), oct 2015. 59
- [29] Teun-Teun Kim, Sang Soon Oh, Hyeon-Don Kim, Hyun Sung Park, Ortwin Hess, Bumki Min, and Shuang Zhang. Electrical access to critical coupling of circularly polarized waves in graphene chiral metamaterials. *Science Advances*, 3(9), September 2017. 60
- [30] Won Jin Choi, Gong Cheng, Zhengyu Huang, Shuai Zhang, Theodore B. Norris, and Nicholas A. Kotov. Terahertz circular dichroism spectroscopy of biomaterials enabled by kirigami polarization modulators. *Nature Materials*, 18(8):820–826, jul 2019. 61
- [31] Longqing Cong, Prakash Pitchappa, Nan Wang, and Ranjan Singh. Electrically programmable terahertz diatomic metamolecules for chiral optical control. *Research*, 2019:1–11, February 2019. 62
- [32] Qianyi Mu, Fei Fan, Sai Chen, Shitong Xu, Chuanzhong Xiong, Xin Zhang, Xianghui Wang, and Shengjiang Chang. Tunable magneto-optical polarization device for terahertz waves based on insb and its plasmonic structure. *Photonics Research*, 7(3):325, February 2019. 63
- [33] Zhiyu Tan, Fei Fan, Dan Zhao, Shanshan Li, Xianghui Wang, and Shengjiang Chang. Linear-polarized terahertz isolator by breaking the gyro-mirror symmetry in cascaded magneto-optical metagrating. *Nanophotonics*, 10(16):4141–4148, October 2021. 64
- [34] Xuewei Ju, Zhiqiang Hu, Guofeng Zhu, Feng Huang, Yanqing Chen, Cuixia Guo, Alexey Belyanin, Junichiro Kono, and Xiangfeng Wang. Creating a near-perfect circularly polarized terahertz beam through the nonreciprocity of a magnetoplasma. *Optics Express*, 31(23):38540, October 2023. 65
- [35] E D Palik and J K Furdyna. Infrared and microwave magnetoplasma effects in semiconductors. *Reports on Progress in Physics*, 33(3):1193–1322, September 1970. 66
- [36] X. Wang, A. A. Belyanin, S. A. Crooker, D. M. Mittleman, and J. Kono. Interference-induced terahertz transparency in a semiconductor magneto-plasma. *Nature Physics*, 6(2):126–130, December 2009. 67
- [37] R. Shimano, Y. Ino, Yu. P. Svirko, and M. Kuwata-Gonokami. Terahertz frequency hall measurement by magneto-optical kerr spectroscopy in inas. *Applied Physics Letters*, 81(2):199–201, July 2002. 68
- [38] B. Paulillo, J. M. Manceau, A. Degiron, N. Zeronian, G. Beaudoin, I. Sagnes, and R. Colombelli. Circuit-tunable sub-wavelength thz resonators: hybridizing optical cavities and loop antennas. *Optics Express*, 22(18):21302, August 2014. 69
- [39] Janine Keller, Giacomo Scalari, Sara Cibella, Curdin Maissen, Felice Appugliese, Ennio Giovine, Roberto Leoni, Matthias Beck, and Jérôme Faist. Few-electron ultrastrong light-matter coupling at 300 ghz with nanogap hybrid lc microcavities. *Nano Letters*, 17(12):7410–7415, November 2017. 70
- [40] Alireza Mottaghizadeh, Yanko Todorov, Mathis Cameau, Djamal Gacemi, Angela Vasanello, and Carlo Sirtori. Nanoscale electromagnetic confinement in thz circuit resonators. *Optics Express*, 25(23):28718, November 2017. 71
- [41] Ian Aupiais, Romain Grasset, Tingwen Guo, Dmitri Daineka, Javier Briatico, Sarah Houver, Luca Perfetti, Jean-Paul Hugonin, Jean-Jacques Greffet, and Yannis Laplace. Ultrasmall and tunable terahertz surface plasmon cavities at the ultimate plasmonic limit. *Nature Communications*, 14(1), November 2023. 72
- [42] Fred Minkowski, Feng Wang, Ayan Chakrabarty, and Qi-Huo Wei. Resonant cavity modes of circular plasmonic patch nanoantennas. *Applied Physics Letters*, 104(2):021111, jan 2014. 73
- [43] Shanhui Fan, Wonjoo Suh, and J. D. Joannopoulos. Temporal coupled-mode theory for the fano resonance in optical resonators. *Journal of the Optical Society of America A*, 20(3):569, March 2003. 74
- [44] J.-M. Manceau, S. Zanotto, I. Sagnes, G. Beaudoin, and R. Colombelli. Optical critical coupling into highly confining metal-insulator-metal resonators. *Applied Physics Letters*, 103(9), August 2013. 75
- [45] Che Qu, Shaojie Ma, Jiaming Hao, Meng Qiu, Xin Li, Shiying Xiao, Ziqi Miao, Ning Dai, Qiong He, Shulin Sun, and Lei Zhou. Tailor the functionalities of metasurfaces based on a complete phase diagram. *Physical Review Letters*, 115(23):235503, December 2015. 76
- [46] Filippo Alpegiani, Nikhil Parappurath, Ewold Verhaegen, and L. Kuipers. Quasinormal-mode expansion of the scattering matrix. *Physical Review X*, 7(2):021035, June 2017. 77

- [47] Hanwen Zhang and Owen D. Miller. Quasinormal coupled mode theory. *arXiv:2010.08650*, 2020. 78
- [48] Mohammed Benzaouia, John D. Joannopoulos, Steven G. Johnson, and Aristeidis Karalis. Quasinormal mode theory of the scattering matrix, enforcing fundamental constraints for truncated expansions. *Physical Review Research*, 3(3):033228, September 2021. 79
- [49] E. Popov, L. Mashev, and D. Maystre. Theoretical study of the anomalies of coated dielectric gratings. *Optica Acta: International Journal of Optics*, 33(5):607–619, May 1986. 80
- [50] M. Nevière, R. Reinisch, and E. Popov. Electromagnetic resonances in linear and nonlinear optics: phenomenological study of grating behavior through the poles and zeros of the scattering operator. *Journal of the Optical Society of America A*, 12(3):513, March 1995. 81
- [51] Felix Binkowski, Fridtjof Betz, Rémi Colom, Patrice Genevet, and Sven Burger. Poles and zeros in non-hermitian systems: Application to photonics. *Physical Review B*, 109(4):045414, January 2024. 82
- [52] Y. D. Chong, Li Ge, Hui Cao, and A. D. Stone. Coherent perfect absorbers: Time-reversed lasers. *Physical Review Letters*, 105(5):053901, July 2010. 83
- [53] Wenjie Wan, Yidong Chong, Li Ge, Heeso Noh, A. Douglas Stone, and Hui Cao. Time-reversed lasing and interferometric control of absorption. *Science*, 331(6019):889–892, February 2011. 84
- [54] William R. Sweeney, Chia Wei Hsu, and A. Douglas Stone. Theory of reflectionless scattering modes. *Physical Review A*, 102(6):063511, December 2020. 85
- [55] Cheryl Feuillet-Palma, Yanko Todorov, Angela Vasanelli, and Carlo Sirtori. Strong near field enhancement in thz nano-antenna arrays. *Scientific Reports*, 3(1), March 2013. 86
- [56] Patrick T. Bowen, Alexandre Baron, and David R. Smith. Theory of patch-antenna metamaterial perfect absorbers. *Physical Review A*, 93(6):063849, June 2016. 87
- [57] P. T. Bowen, A. Baron, and D. R. Smith. Effective-medium description of a metasurface composed of a periodic array of nanoantennas coupled to a metallic film. *Physical Review A*, 95(3):033822, March 2017. 88
- [58] Jiangfeng Zhou, Dibakar Roy Chowdhury, Rongkun Zhao, Abul K. Azad, Hou-Tong Chen, Costas M. Soukoulis, Antoinette J. Taylor, and John F. O'Hara. Terahertz chiral metamaterials with giant and dynamically tunable optical activity. *Physical Review B*, 86(3):035448, jul 2012. 89
- [59] M. G. Moharam, T. K. Gaylord, Eric B. Grann, and Drew A. Pommet. Formulation for stable and efficient implementation of the rigorous coupled-wave analysis of binary gratings. *Journal of the Optical Society of America A*, 12(5):1068, May 1995. 90
- [60] Jean Paul Hugonin and Philippe Lalanne. Reticolo software for grating analysis. *arXiv:2101.00901*, 2021. 91
- [61] Y. Todorov, L. Tosetto, J. Teissier, A. M. Andrews, P. Klang, R. Colombelli, I. Sagnes, G. Strasser, and C. Sirtori. Optical properties of metal-dielectric-metal microcavities in the thz frequency range. *Optics Express*, 18(13):13886, June 2010. 92